3D pyrography as a process tunable feature in polylactic acid/olive wood composite material extrusion

Francisco Comino and *Jose A. Martínez-Sánchez*
Departamento de Mecánica, Escuela Politécnica Superior, Universidad de Córdoba, Campus de Rabanales, Córdoba, España, and
Roberto Spina
Dipartimento di Meccanica, Matematica e Management (DMMM), Politecnico di Bari, Bari, Italy, and Istituto Nazionale di Fisica Nucleare (INFN) – Sezione di Bari, Politecnico di Bari, Bari, Italy

Abstract

Purpose – This study aims to investigate polylactic acid (PLA)/olive wood (PLA/OW) composites for material extrusion (MEX) and frames 3D pyrography as a process-tunable surface appearance feature, linking printing conditions to surface texture and colour.

Design/methodology/approach – PLA/OW filaments (0–20 Wt.% OW) were compounded and printed while varying extrusion temperature and printing speed. FTIR, differential scanning calorimeter and thermogravimetric analysis supported thermo-chemical assessment and oscillatory rheology aided printability evaluation. Surface texture was quantified by confocal areal roughness, and colour was measured in CIELAB and expressed as ΔE00. Multifactor analysis of variance and second-order response surfaces were used to map process–appearance relationships within the tested range.

Findings – Increasing OW reduced crystallinity and thermal stability and increased melt viscoelasticity, narrowing the practical processing window. Roughness rose with OW content and was further governed by printing conditions. Temperature dominated chromatic change, promoting darkening (lower L*) and higher ΔE00, whereas higher printing speeds reduced thermal exposure and helped preserve lighter shades. The response surfaces provide consistent maps for combined texture–colour tuning.

Practical implications – The approach can support aesthetic tuning using a single biofilled filament, potentially reducing the need for multiple coloured materials, filament changeovers and purge-related waste in design-oriented MEX applications.

Originality/value – This work provides a quantitative framework that treats 3D pyrography in PLA/OW as a controllable process feature, jointly mapping colour (CIELAB/ΔE00) and surface texture as outcomes of MEX parameters, enabling reproducible tone modulation without post-processing.

Keywords Material extrusion, Biocomposites, Surface roughness, CIELAB, CIEDE2000, Process mapping, Sustainable materials

Paper type Research paper

1. Introduction

Material extrusion (MEX) additive manufacturing (AM) is increasingly used beyond rapid prototyping for design-oriented production, driven by geometric flexibility, short lead times and efficient material use (Turner *et al.*, 2014). Polylactic acid (PLA) has become the main polymer in this process due to its biobased origin and better printability compared to typical thermoplastics (Tao *et al.*, 2017). In parallel, efforts to reduce environmental impact have encouraged the use of lignocellulosic fillers such as wood flour and agroforestry fibres, which can lower cost and embodied energy while providing a natural visual and tactile finish (Ehman *et al.*, 2025). These fillers can be incorporated through filament compounding and MEX when particle size and moisture levels are properly controlled; however, they also introduce interfacial and rheological challenges, often causing voids, particle pull-out and higher surface roughness, reinforcing the strong coupling between processing conditions and surface quality (Le Guen *et al.*, 2019; dos Santos *et al.*, 2025). Among these fillers, olive wood (OW) waste is especially important in Mediterranean regions, where the olive industry produces large amounts of

The current issue and full text archive of this journal is available on Emerald Insight at: **https://www.emerald.com/insight/1355-2546.htm**

Rapid Prototyping Journal
32/11 (2026) 163–180
Emerald Publishing Limited [ISSN 1355-2546]
[DOI 10.1108/RPJ-01-2026-0065]

Funding: The authors acknowledge the financial support from the European Innovation Association (AEI) for agricultural productivity and sustainability, which facilitated the creation and operation of operational groups, as well as support from the Ministry of Agriculture, Livestock, Fisheries, and Sustainable Development of the Junta de Andalucía through the research project AGROSEC, reference GOPO-JA-23. The project was additionally funded by the National Recovery and Resilience Plan (NRRP), Mission 4, Component 2, Investment 1.3, under Call for tender No. 341 of 03/15/2022 by the Italian Ministry of University and Research (MUR), financed by the European Union – NextGenerationEU.

Received 3 February 2026
Revised 6 April 2026
11 June 2026
Accepted 28 July 2026

low-value by-products (Lo Giudice *et al.*, 2021; Taktak *et al.*, 2023). Valorizing OW in PLA therefore supports circular-economy strategies while enabling wood-like aesthetics that can be tuned during printing (Fico *et al.*, 2022).

Wood-filled PLA filaments for MEX have been repeatedly demonstrated as feasible, provided particle size and moisture are carefully controlled to avoid nozzle clogging and melt-flow instabilities. Practical guidelines recommend particles smaller than the nozzle diameter and thorough drying during extrusion and printing (Khan *et al.*, 2025). However, increasing wood content commonly promotes voids, agglomeration and particle pull-out, particularly under suboptimal deposition settings or weak interfacial bonding, leading to rougher surfaces and more pronounced raster marks (Boschetto *et al.*, 2013; Kariz *et al.*, 2018). Despite these constraints, applications have expanded from functional prototypes to design-driven products, including acoustic panels (Sheng *et al.*, 2024) and heat- or mass-exchange devices (Comino *et al.*, 2023; Martínez-Sánchez *et al.*, 2025). Pilot-scale dual-material concepts have further shown that varying wood content within a single part can be used to tailor appearance and functionality (Jaróg *et al.*, 2025). Overall, PLA/wood systems have become a practical design material, although printability remains strongly dependent on morphology and surface quality (Mirza *et al.*, 2025).

The mechanical behaviour of PLA/wood composites has been extensively studied, typically showing a trade-off between stiffness and toughness, where low to moderate wood contents increase modulus but higher loadings reduce strength and ductility due to dispersion limits, porosity and particle pull-out (Bharat *et al.*, 2025; Sultana *et al.*, 2024; Travieso-Rodriguez *et al.*, 2021). These trends highlight the role of microstructure and interfacial quality, which are also directly reflected in surface morphology and printing quality (Liu *et al.*, 2019).

On the rheological side, PLA/wood systems have been less discussed in MEX literature compared to their mechanical behaviour (Lee *et al.*, 2021). Adding wood generally increases melt elasticity and complex viscosity, which can narrow the practical processing window when particle size, dispersion and moisture are not properly controlled during filament preparation and printing (Jasiński *et al.*, 2025). These factors directly affect nozzle stability, flow continuity and inter-bead coalescence during deposition (Sun *et al.*, 2008). Thermo-rheological studies on cellulose-reinforced PLA reported increasing storage modulus (G') and complex viscosity with filler content while preserving shear-thinning behaviour, indicating reduced chain mobility and a greater sensitivity to extrusion temperature for achieving adequate bonding without thermal overstressing (Awal *et al.*, 2015).

The thermal behaviour of PLA/wood composites has been examined in several studies (Comino *et al.*, 2025). Differential scanning calorimetry (DSC) typically shows nearly constant melting temperatures but decreasing crystallinity with increasing wood loading, indicating limited chain packing and altered solidification behaviour (Taktak *et al.*, 2024). The glass transition temperature often shifts slightly to lower values, consistent with interfacial heterogeneity and increased free volume at polymer–filler boundaries. Thermogravimetric analysis (TGA) commonly reveals reduced onset and peak degradation temperatures compared to neat PLA, together with higher char residue due to the lignocellulosic fraction, highlighting the need for careful temperature selection during MEX processing (Petinakis *et al.*, 2010; Taktak *et al.*, 2024). These thermal trends support defining a material-specific processing window for PLA/OW to balance appearance tuning and defect avoidance.

In MEX-produced PLA/wood parts, layer height, bead width, extrusion temperature and printing speed govern melt flow, bead coalescence and surface quality formation. Insufficient heat input leads to limited inter-filament diffusion and raster undulations (Sun *et al.*, 2008), whereas excessive input promotes local instabilities and defects. Both mechanisms increase surface roughness and anisotropy, making process control critical for repeatable surface texture (Yang and Yeh, 2020). In addition to texture, the optical appearance of lignocellulosic composites is also process dependent (Kariz *et al.*, 2018). While wood content sets the baseline tone, recent demonstrations of 3D-printed pyrography using wood filaments show that printing conditions can be used to intentionally modulate colour, commonly quantified in the *CIELAB space* (L^*, a^*, b^*) (ISO, 2019; Moon *et al.*, 2024). Similar parameter-driven effects have been reported even in neat PLA, where flow rate, nozzle temperature and cooling reshape raster geometry and heat transfer, producing mainly lightness-controlled (grayscale) changes rather than hue variations (Spina, 2025). Nevertheless, material-specific frameworks that jointly map processing conditions to both surface texture and colour development remain limited.

Although prior research has demonstrated the feasibility of wood-filled PLA for MEX and documented how processing influences morphology, PLA/OW-specific frameworks that translate deposition parameters into actionable texture–colour outcomes while respecting thermal constraints remain limited. Studies on OW and similar lignocellulosic systems have reported spectral and thermal trends. However, they have rarely been integrated into design-oriented process maps that connect deposition conditions with optical response. Likewise, surface-quality studies in additive manufacturing often focus on parameter control but seldom quantify surface texture and colour simultaneously within a unified methodology. Moreover, statistically supported PLA/OW correlations linking temperature and printing speed to CIELAB coordinates and ΔE00 together with surface texture are still missing. This research addresses that gap by treating 3D pyrography in PLA/OW as a process-tunable design feature, combining

- surface texture quantification;
- thermo-chemical support of the processing window using FTIR, DSC and TGA; and
- analysis of variance (ANOVA)-supported empirical response-surface mapping of extrusion temperature and printing speed against CIELAB colour coordinates.

This work aims to establish 3D pyrography as a process-tunable optical function in PLA/OW parts produced by MEX, linking composition and printing parameters to surface texture and colour within a thermally supported processing window. To achieve this:

- PLA/OW filaments (0–20 Wt.% OW) were developed and characterized through spectroscopy, calorimetry, thermogravimetry and rheology to assess material integrity and printability;

- microstructure and primary surface texture were quantified and DOE-based ANOVA response surfaces were used to relate extrusion temperature and printing speed to CIELAB coordinates and ΔE00 within the tested range; and
- the results were translated into process maps identifying combined roughness and lightness trends, enabling controlled darkening and demonstrated through proof-of-concept, process-controlled tonal patterns.

2. Materials and methods

2.1 Materials and PLA/OW filament manufacturing

A series of composite filaments was formed by adding OW particles into a PLA matrix. Five formulations were created: neat PLA, PLA/OW05 (5 Wt.% OW), PLA/OW10 (10 Wt.% OW), PLA/OW15 (15 Wt.% OW) and PLA/OW20 (20 Wt.% OW). The filler loadings were chosen to span a range of compositions while maintaining good printability in MEX without needing extra processing aids or compatibilizers.

The polymer matrix used was Luminy LX175 (TotalEnergies Corbion, The Netherlands) (TotalEnergies Corbion, 2022), a commercial-grade PLA. The OW particles were produced as a by-product of pruning (Figure 1), then milled and sieved to obtain fractions with particle sizes less than 180 μm. This granulometry was chosen to ensure continuous extrusion without clogging or filament breakage.

Before compounding, PLA pellets and OW particles were dried at 60°C for 12 h to reduce moisture below 2 Wt.% and minimize hydrolytic degradation. Composite blends were prepared by gravimetric dosing and compounded in a co-rotating twin-screw extruder using a temperature profile of 170–190–200°C. The extrudate was pelletized and converted into 1.75 ± 0.03 mm filaments using a single-screw extruder under controlled temperature and draw conditions to ensure dimensional stability.

2.2 Morphology and composition characterization

The morphological characterization of the filament surfaces was performed using a JSM6300 scanning electron microscope (SEM) (Jeol Ltd., Japan). Before observation, the samples were sputter-coated with a thin layer of gold to prevent surface charging. Micrographs were captured at an accelerating voltage of 5 kV and at various magnifications, with primary analysis conducted at 100 × using a 100 μm scale bar to assess overall morphology and defect distribution. Image analysis and quantitative defect evaluation were performed using ImageJ and the full processing workflow is reported in the Supplementary material (Section S1).

FTIR spectra were obtained using a Tensor 27 spectrometer (Bruker Optik GmbH, Germany) within the 4,000–400 cm^{-1} range to examine the chemical composition and possible interactions between the polymer matrix and the OW fibres. Filament segments (neat PLA and PLA/OW 5–20 Wt.%) were analysed directly without any chemical preparation. Spectra were exported as absorbance values and automatically baseline-corrected, without smoothing. For visual comparison, the spectra displayed were vector-normalized to unit intensity.

Figure 1 Olive wood particles from pruning

Source: Authors' own work

2.3 Thermal characterization

The thermal behaviour of neat PLA and PLA/OW composites was studied using a DSC with a DSC 404 F3 Pegasus, equipped with a silver furnace (Netzsch-Gerätebau GmbH, Germany). About 5 mg of each sample was weighed and hermetically sealed in standard aluminium pans.

Each test involved a heating–cooling–heating cycle to reset the material's thermal history and obtain consistent thermal parameters. The protocol was:

- first heating from 25°C to 200°C at 10°C/min to relieve residual stresses and clear the processing history;
- cooling to 25°C at 10°C/min under a nitrogen atmosphere; and
- second heating from 25°C to 200°C at 10°C/min, during which the glass transition temperature T_g, melting temperature T_m and enthalpy of fusion ΔH_m were measured.

The degree of crystallinity X_c was calculated using equation (1), where ΔH_m is the measured enthalpy, ΔH_m^0 is the melting enthalpy of 100% crystalline PLA (93 J/g) and w_f is the weight fraction of olive wood particles in the composite. In this work, X_c was calculated on the basis of the composite total mass (i.e. not normalized by the PLA fraction). This approach was used to allow a direct comparison between neat PLA and the PLA/OW composites. All measurements were repeated three times and the reported values represent the average ± standard deviation:

$$X_c = \frac{\Delta H_m}{\Delta H_m^0 \ (1\text{-}w_f)} \cdot 100 \quad (1)$$

Thermal stability was evaluated using TGA with an SDT Q600 instrument (TA Instruments, USA). Approximately 15 mg of each sample was heated from 10°C to 600°C at a heating rate of 10°C/min under a nitrogen atmosphere.

2.4 Rheological characterization

The material behaviour was assessed by measuring rheological properties with a HAAKE Mars rotational rheometer (ThermoScientific Inc., USA) to examine flow behaviour during extrusion. The storage G' and loss G'' moduli were recorded as frequency from 1 to 100 rad/s, using 1% strain, a 0.5 mm gap and a fixed test temperature. Based on the G' and

G'' data, the complex viscosity η^* was calculated using equation (2), where ω is the angular frequency (rad/s):

$$\eta^* = \frac{1}{\omega} \cdot \sqrt{G'^2 + G''^2} \quad (2)$$

2.5 Surface and colour characterization

The surfaces of the specimens were examined using a DCM8 confocal microscope (Leica GmbH, Germany), in accordance with ISO 25178 standards. The surfaces of neat PLA and composites with varying OW content were initially analysed to assess how filler content influences surface roughness. Discs with a diameter of 20 mm were printed using an X1C MEX printer (Bambu Lab, China) under identical processing conditions and representative flat regions were scanned to measure the areal parameters. These include the arithmetic mean height S_a, the root-mean-square height S_q and the maximum height S_z, as defined in ISO 25178. The printing parameters are summarized in Table 1. In the subsequent analysis, the effect of printing parameters was examined by adjusting the extrusion temperature (180–280°C) and printing speed (20–200 mm/s), while keeping the remaining settings constant. These parameters were selected because inter-filament bonding and bead coalescence in MEX are primarily thermally driven and strongly depend on nozzle temperature and deposition rate (Sun *et al.*, 2008). The extrusion-temperature range (180–280°C) was selected based on processing considerations for MEX rather than on service temperatures of the final parts. The lower bound (180°C) was chosen as the minimum temperature that still ensured stable melting and deposition of the PLA-based filament, whereas the upper bound (280°C) was selected to explore the onset of thermally induced colour darkening (3D pyrography) while remaining below the initial degradation range identified by TGA. Therefore, the selected interval was intended to span the practical processing window of the PLA/OW system, from stable extrusion conditions to severe, but still printable, thermal exposure conditions. PLA-based specimens printed under these conditions were characterized using the confocal method to evaluate the relationship between process parameters and surface texture.

Table 1 Printing parameters

Parameter	Value
Layer height (mm)	0.2
Layer width (mm)	0.4
Raster angle (°)	45
Infill density (%)	100
Infill pattern	Line
Printing speed (mm/s)	20–200
Flow (%)	100
Nozzle diameter (mm)	0.4
Extrusion temperature (°C)	180–280
Build plate temperature (°C)	65
Build orientation	Horizontal (XY)

Source(s): Authors' own work

No separate heat-treatment stage was considered in this work. Thermal exposure occurred exclusively during MEX processing and was controlled by the combined effect of nozzle temperature and deposition rate. Therefore, at a given extrusion temperature, lower printing speed results in longer effective thermal exposure, while higher printing speed shortens the exposure time.

Images of printed surfaces were captured under controlled lighting to qualitatively evaluate homogeneity, colour tone and visible defects, such as cracks or filament raster marks. These observations helped determine the initial condition of the specimens and supported the subsequent interpretation of pyrography results.

Visible absorbance spectra in the 400–700 nm range were also obtained using a NIRSystems DS2500 spectrometer (FOSS, Denmark). The same discs were used for this measurement. From the absorbance data $A(\lambda)$, the spectral reflectance $R(\lambda)$ was calculated using equation (3), following the standard definition of absorbance in diffuse reflectance measurements:

$$R(\lambda) = 10^{A(\lambda)} \quad (3)$$

Colour coordinates were calculated following the recommendations of the Commission Internationale de l'Éclairage (CIE) (ISO, 2019). Reflectance spectra were combined with the spectral power distribution of illuminant A (2856 K) and the colour-matching functions of the CIE 1931 2° standard observer to obtain the tristimulus values (X, Y, Z). The corresponding CIELAB coordinates (L^*, a^*, b^*) were then computed using the CIE non-linear transformations. The complete calculation procedure and equations are provided in the Supplementary material (Section S2).

This procedure yielded the parameters L^*, a^* and b^*, which provided an objective quantification of the colour variation of the samples as a function of processing conditions.

A multifactorial experimental design (DOE) was also used to evaluate how extrusion temperature T and printing speed V influence the colour parameters L^*, a^* and b^* of the composites. Centurion software (Statgraphics Technologies Inc., USA) was used for statistical analysis. The DOE included three levels of extrusion temperature (180, 240 and 280°C) and two levels of printing speed (20 and 200 mm/s), resulting in a 3×2 factorial design. For each combination of extrusion temperature and printing speed, 3 independently printed specimens were analysed and the colour coordinates used in the ANOVA corresponded to the average values obtained from these replicate measurements. The residual error term in the ANOVA was estimated from the variability among these independent replicates. This analysis focused on the PLA/OW05 formulation as a representative system to identify general trends in colour variation based on processing parameters. Similar patterns were seen with higher filler loadings, confirming that PLA/OW05 is a suitable baseline for the statistical analysis.

The experimental results were analysed using ANOVA to determine the significance of the main factors (T and V) and their interactions ($T{\cdot}T$ and $T{\cdot}V$). In addition, polynomial regression models were developed to predict L^*, a^* and b^* as a function of the input variables. The models followed the standard second-order polynomial form commonly used in response surface methodology, as shown in equation (4), where $\widehat{Y_r}$ was the estimated response, X_r were input variables, c_i, c_{ii} and c_{ij} were the

coefficients of the linear, quadratic and interaction terms, respectively, and c_0 was the intercept (Montgomery, 2004):

$$\widehat{Y_r} = c_0 + \sum_{i=1}^{l} c_i \cdot X_{r,i} + \sum_{i=1}^{l} c_{ii} \cdot X_{r,i}^2 + \sum_{i=1}^{l=1} \sum_{\substack{i=2 \\ j>i}}^{l} c_{ij} \cdot X_{r,i} \cdot X_{r,j} \quad (4)$$

Colour differences between samples and their reference condition (180°C, 20 mm/s for each material) were quantified using the CIEDE2000 ΔE_{00} formula (Sharma *et al.*, 2005). This approach, recommended by the CIE (ISO, 2019), accounts for perceptual non-uniformities in the CIELAB space by introducing corrections for lightness, chroma and hue. The total colour difference ΔE_{00} was computed from the CIELAB coordinates of each sample and its reference using equation (5), where $\Delta L'$, $\Delta C'$ and $\Delta H'$, were the differences in lightness, chroma and hue between the sample and the reference S_L, S_C and S_H were weighting functions that normalized these components, R_T was a rotation term accounting for the interaction between chroma and hue differences and $k_L = k_C = k_H = 1$ under reference conditions:

$$\Delta E_{00} = \sqrt{\left(\frac{\Delta L'}{k_L S_L}\right)^2 + \left(\frac{\Delta C'}{k_C S_C}\right)^2 + \left(\frac{\Delta H'}{k_H S_H}\right)^2 + R_T \left(\frac{\Delta C'}{k_C S_C}\right) \left(\frac{\Delta H'}{k_H S_H}\right)} \quad (5)$$

3. Results and discussion

3.1 Morphology analysis

Figure 2 presents SEM micrographs of neat PLA and PLA/OW composites. To facilitate interpretation, the representative fracture-surface features identified in Figure 2 have been marked directly on the SEM micrographs, including cavities/voids, pull-out traces and heterogeneous regions associated with matrix–particle debonding. Neat PLA exhibited a relatively smooth fracture surface with no large cavities (>10 μm), indicating a uniform matrix. With increasing OW content, the fracture surfaces became progressively more heterogeneous, with a higher density of cavities and pull-out traces consistent with particle debonding and limited interfacial adhesion. Defect size and irregularity increased from microcavities typically below 20 μm at 5 Wt.% OW to elongated cavities and pull-out imprints in the 30–50 μm range at 10 Wt.% OW and to defects exceeding 50 μm at 20 Wt.% OW. Overall, OW addition promoted a gradual transition from a continuous fracture surface to a rougher morphology dominated by voids and interfacial heterogeneities, which is consistent with the observed reduction in mechanical integrity at higher filler contents.

3.2 Infrared spectra

Figure 3 shows the FTIR spectra of pure PLA and PLA/OW composites, with the main absorption bands listed in Table 2. The spectrum of pure PLA exhibits characteristic bands of the polyester matrix, including the strong carbonyl stretching at 1,745 cm^{-1}, the asymmetric and symmetric C–H stretching bands at 2,940 cm^{-1} and 2,860 cm^{-1}, respectively, and the C–O–C stretching vibration at 1,080 cm^{-1}. The band at 1,465 cm^{-1} corresponds to the bending of $-CH_3$ groups, while signals at 870 cm^{-1} are related to crystalline domains of PLA.

In the composites, new absorption features appeared, attributed to the addition of OW particles. Notably, the broad band at 3,440 cm^{-1} grew stronger as the filler amount increased, indicating the O–H stretching vibrations of hydroxyl groups found in cellulose, hemicellulose and lignin. In addition, two distinct bands at 1,558 cm^{-1} and 1,515 cm^{-1} emerged, representing the aromatic skeletal vibrations of lignin, which were absent in pure PLA. The increased intensity of these lignin-related peaks with higher OW loadings confirmed the successful integration of lignocellulosic components.

The gradual increase in the intensity of the hydroxyl (O–H) and aromatic (C = C) bands with filler content clearly indicated the presence of wood particles within the PLA matrix. Conversely, the intensity of the carbonyl peak at 1,745 cm^{-1} slightly diminished in the composites compared to neat PLA, suggesting that the PLA ester groups were partially masked by the wood particles and their hydroxyl-rich surface.

These results aligned with previous studies on PLA/OW composites (Fico *et al.*, 2022; Taktak *et al.*, 2023, 2024), which also showed the preservation of PLA's main absorptions along with intensified O–H and aromatic bands from lignocellulosic components, confirming the successful incorporation of OW particles into the polymer matrix.

3.3 Thermal analysis

Figure 4 shows the DSC thermograms of neat PLA and PLA/OW composites. The thermal parameters, including T_g, T_m, ΔH_m and X_c, are summarized in Table 3.

The glass transition temperature T_g of neat PLA was measured at 62.0°C, while the composites showed progressively lower T_g values with increasing OW content, reaching 58.2°C in PLA/OW20. These decreases indicated that adding OW particles reduced the mobility restrictions on PLA chains, possibly by creating interfacial free volume and partially disrupting chain–chain interactions. The reduction in T_g with filler addition has been reported in other PLA-based composites containing lignocellulosic fibres. It has been attributed to local heterogeneities at the interface between hydrophilic fillers and the hydrophobic PLA matrix (Kariz *et al.*, 2018; Tao *et al.*, 2017).

The melting temperature T_m remained nearly constant (149.9–151.2°C), indicating that OW did not markedly alter the lamellar thickness of PLA crystals. In contrast, the enthalpy of fusion decreased with OW loading and X_c dropped from 25.5% (neat PLA) to 14.8% (PLA/OW20), indicating that the presence of OW hindered crystal growth and reduced crystalline perfection. This behaviour can be attributed to the increasing interfacial heterogeneity introduced by the lignocellulosic particles, which disrupts the regular packing of PLA chains and limits their rearrangement into ordered crystalline domains during solidification. In addition, the higher melt viscoelasticity observed for the composites may further restrict the reorganization of PLA chains required for crystallization. Overall, OW addition decreased T_g and crystallinity while preserving T_m, consistent with increased interfacial heterogeneity in PLA/OW systems (Kariz *et al.*, 2018; Tao *et al.*, 2017).

Figure 2 SEM images of (a) neat PLA, (b) PLA/OW05, (c) PLA/OW10 and (d) PLA/OW20. The marked regions indicate representative morphological features observed in the fracture surfaces, including cavities/voids, pull-out traces and heterogeneous areas associated with increasing OW content

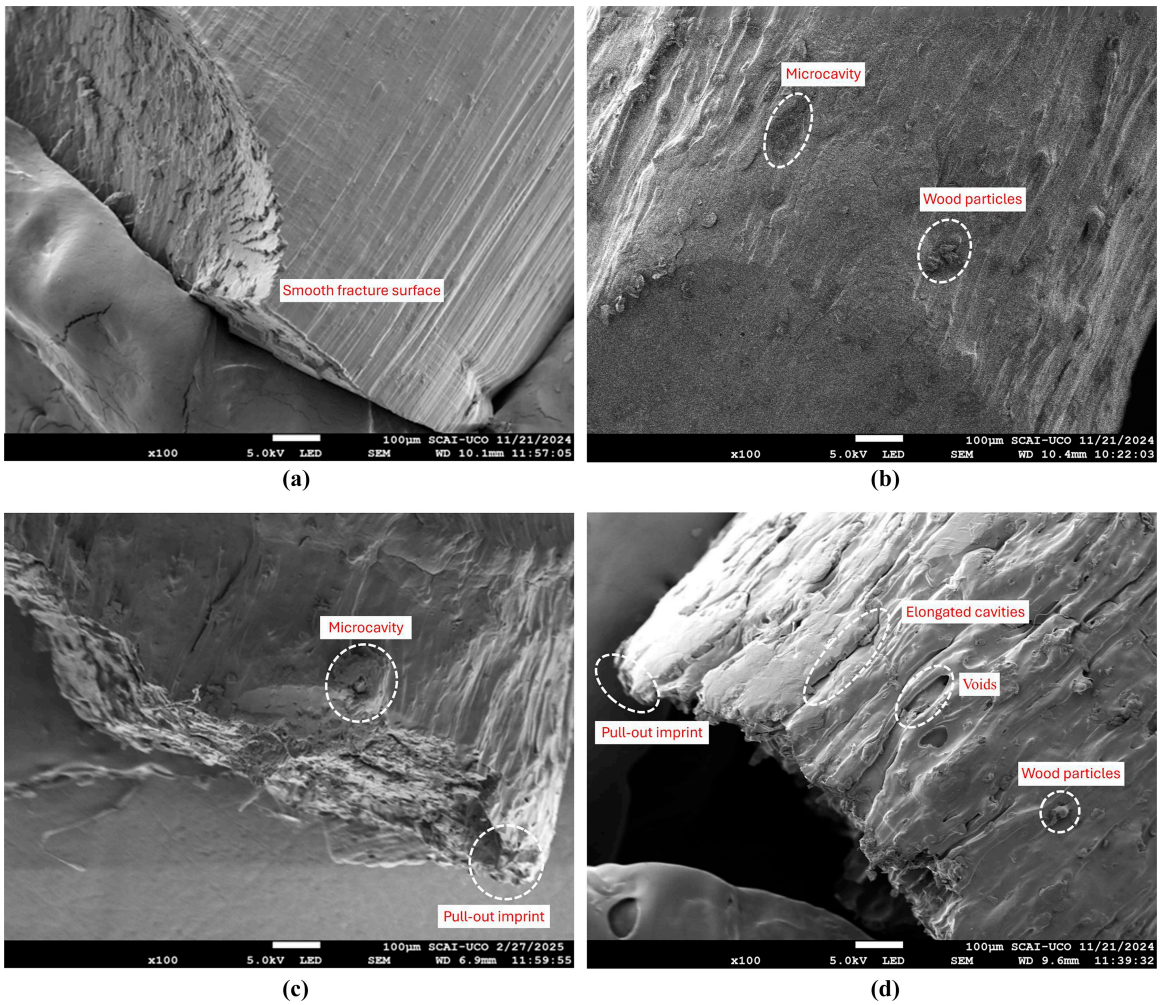

Source: Authors' own work

Therefore, the DSC results confirmed that increasing OW content modified the thermal behaviour of PLA mainly by reducing T_g and crystallinity, while leaving T_m almost unchanged. These findings highlight the influence of filler–matrix interactions on the structural organization of the polymer and indicate that high OW levels hinder the development of ordered crystalline regions in the PLA matrix.

Figure 5 shows the TGA curves of neat PLA and PLA/OW composites. At the same time, Table 4 summarizes the main thermal degradation parameters, namely, the temperature at which the material has lost 5% of its mass ($T_{5\%}$), the maximum degradation temperature (T_{max}, corresponding to the temperature at which the maximum rate of thermal degradation occurs) and the final residual weight (at 580°C).

Neat PLA showed single-step degradation with $T_{5\%} = 344.9$°C and $T_{max} = 375.9$°C. Increasing OW content shifted both temperatures to lower values ($T_{5\%} = 293.2$°C and $T_{max} = 348.3$°C for PLA/OW20), indicating reduced thermal stability due to the earlier decomposition of lignocellulosic components and the presence of thermally labile hydroxyl groups (Kariz *et al.*, 2018; Tao *et al.*, 2017). Conversely, the residue at 580°C increased from 0.2% (PLA) to 7.5% (PLA/OW20), consistent with char formation from the lignin-rich fraction (Zhou *et al.*, 2022).

3.4 Rheological analysis

Figures 6–8 show the curves of G', G'' *and* η^* of the polymers with OW content ranging from 0% (neat PLA) to 10% as a function of shear rate ω. The data consisted of measured rheological data (scatters) and curves fitted using the Carreau–Yasuda model. The complex viscosity decreased with increasing shear rate for all materials, indicating typical pseudoplastic (shear-thinning) behaviour. Polymeric chains were arranged in a random or entangled configuration at low shear rates, resulting in high viscosity. Newtonian-like plateaus were observed at higher temperatures for η^* across different OW contents, but they ended at lower frequencies. The subsequent decay with frequency was steeper, with a more solid-like behaviour at higher frequencies, due to less time for the polymer chain disentanglement. As the shear rate increased, the polymeric chains experienced greater

Figure 3 FTIR spectra of PLA and PLA/OW composites

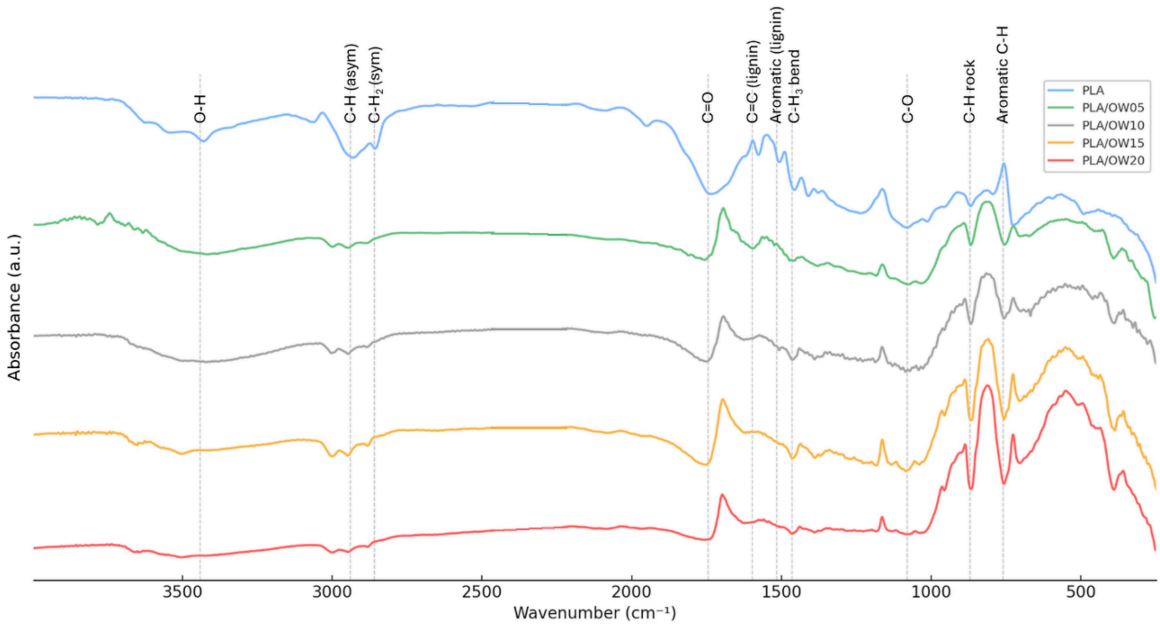

Source: Authors' own work

Table 2 Main FTIR absorption bands of PLA and PLA/OW composites

Wavenumber (cm^{-1})	Assignment	Origin
3,440	O–H stretching	Hydroxyl groups (cellulose, hemicellulose, lignin)
2,940	C–H asymmetric stretching (CH_3/CH_2)	PLA backbone and wood polysaccharides
2,860	C–H_2 symmetric stretching	PLA and wood polysaccharides
1,745	C = O stretching (ester carbonyl)	PLA
1,558	Aromatic C = C stretching	Lignin
1,515	Aromatic skeletal vibrations	Lignin
1,465	C–H bending (CH3 asymmetric deformation)	PLA (with contributions from wood)
1,080	C–O stretching (C–O–C, polysaccharides)	PLA and wood (cellulose/hemicellulose)
870	C–H rocking/skeletal vibration	PLA crystalline domains
760	Aromatic C–H out-of-plane bending	Lignin

Source(s): Authors' own work

deformation, leading to disentanglement and alignment in the flow direction while reducing viscosity.

As shown in Figure 6–8, the addition of OW increased G', G'' and η^* over the whole frequency range, with PLA/OW10 showing the highest viscoelastic response. This behaviour indicates that the lignocellulosic particles restricted the mobility and rearrangement of PLA chains in the melt, increasing flow resistance and promoting a more structured viscoelastic response. Similar trends have been reported for cellulose-reinforced PLA systems, in which filler incorporation increased storage modulus and complex viscosity while preserving shear-thinning behaviour (Awal *et al.*, 2015). Comparable effects have also been observed in wood-filled PLA composites, where the presence of rigid lignocellulosic particles hindered melt flow and made the rheological response strongly dependent on filler–matrix interactions and dispersion quality (Yue *et al.*, 2022).

In addition, the more pronounced low-frequency response observed with increasing OW content suggests the development of stronger filler–matrix interactions and possible transient particle networks or agglomerated structures within the melt. A similar interpretation has been proposed for PLA/cellulosic systems, where the upward deviation at low frequency has been associated with network formation and enhanced melt structuring (Cui *et al.*, 2021). In the present case, this rheological behaviour was not detrimental to printability. On the contrary, the increase in viscoelasticity may contribute to better shape retention after deposition, although it also implies a narrower practical processing window as OW loading increases.

3.5 Surface analysis

Figure 9 presents representative 3D topographies for PLA/OW05 and PLA/OW20 and Table 5 summarizes the superficial

Figure 4 DSC for PLA and PLA/OW composites

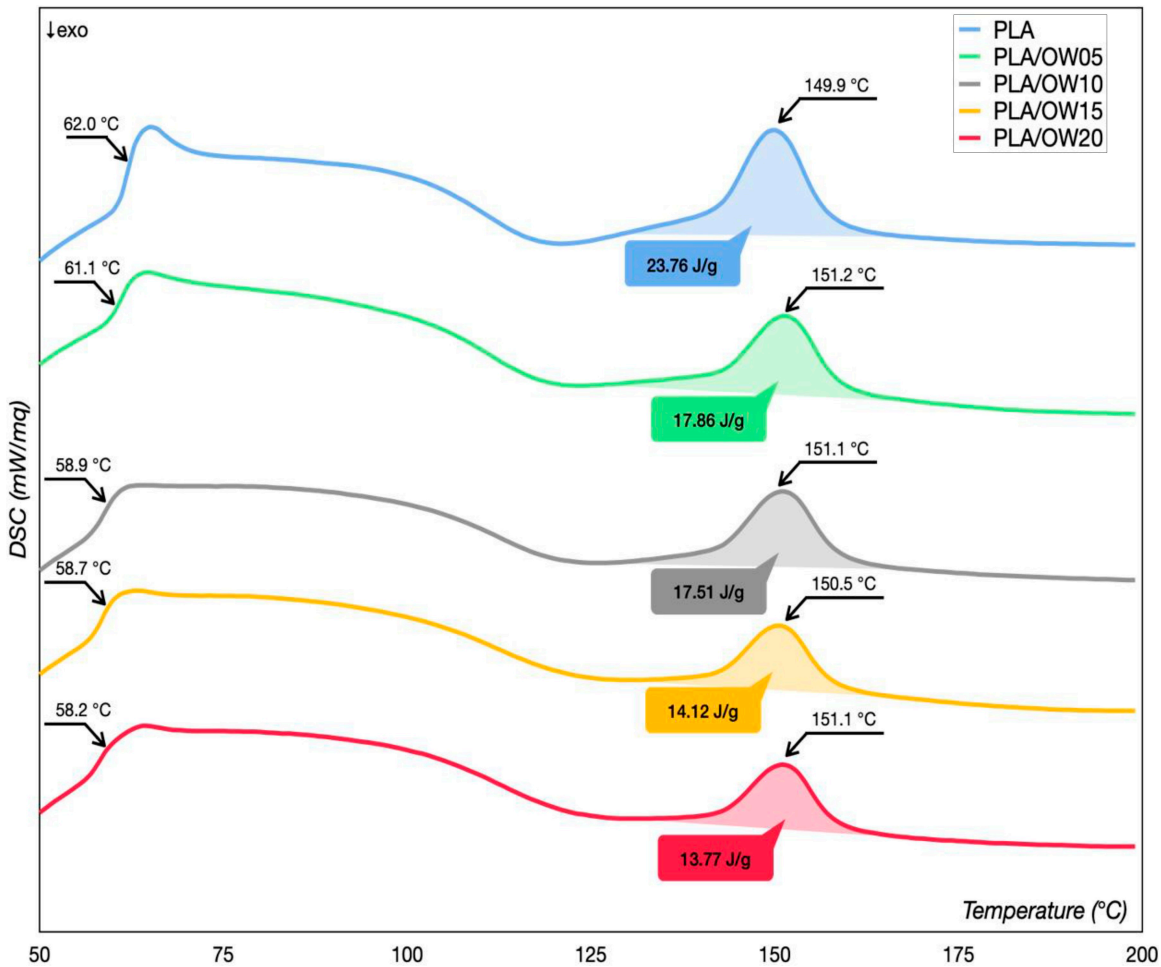

Source: Authors' own work

Table 3 DSC parameters of PLA and PLA/OW composites

Material	T_g (°C)	T_m (°C)	ΔH_m (J/g)	X_c (%)
Neat PLA	62.0	149.9	23.76	25.5
PLA/OW05	61.1	151.2	17.86	19.2
PLA/OW10	58.9	151.1	17.51	18.8
PLA/OW15	58.7	150.5	14.12	15.2
PLA/OW20	58.2	151.1	13.77	14.8

Source(s): Authors' own work

parameters S_a, S_q and S_z for all formulations. The characterization of the primary surface of the MEX specimens, evaluated according to ISO 25178, revealed a systematic increase in amplitude with increasing OW content. The visual comparison of the 3D topographies in Figure 9 corroborated this transition from a relatively homogeneous surface (PLA/OW05) towards a more irregular and heterogeneous landscape (PLA/OW20).

Neat PLA exhibited baseline values of $S_a = 3.59\,\mu$m, $S_q = 5.01\,\mu$m and $S_z = 42.32\,\mu$m. From these values, the incorporation of OW led to a nearly monotonic increase in mean and quadratic roughness up to 15 Wt.%, with $S_a = 3.76$, 4.57 and 5.38 μm and $S_q = 5.08$, 6.05 and 7.41 μm for PLA/OW05, PLA/OW10 and PLA/OW15, respectively, corresponding to increases of 4.7–49.9% in S_a and 1.4–47.9% in S_q compared to PLA. Between 15 and 20 Wt.%, a slight plateau was observed ($S_a = 5.39\,\mu$m; $S_q = 7.52\,\mu$m), suggesting that, once a critical particle surface coverage was reached, further loading did not uniformly elevate the surface profile but instead resulted in localized irregularities.

S_z proved to be the most sensitive parameter to filler content, rising from 48.56 μm in PLA/OW05 to 76.40 μm in PLA/OW20, which represented an overall increase of 80.6% compared with PLA (42.32 μm). This pronounced growth in extreme peak-to-valley height indicated a higher frequency of sharp asperities and deep valleys with increasing OW content, consistent with the exposure of particles and agglomerates at the free surface, the formation of pull-out voids and the incomplete coalescence of filaments due to increased melt viscosity and reduced interdiffusion during deposition. The increase in roughness parameters with OW content was aligned with previous findings (Yang and Yeh, 2020), who reported

Figure 5 TGA for PLA and PLA/OW composites

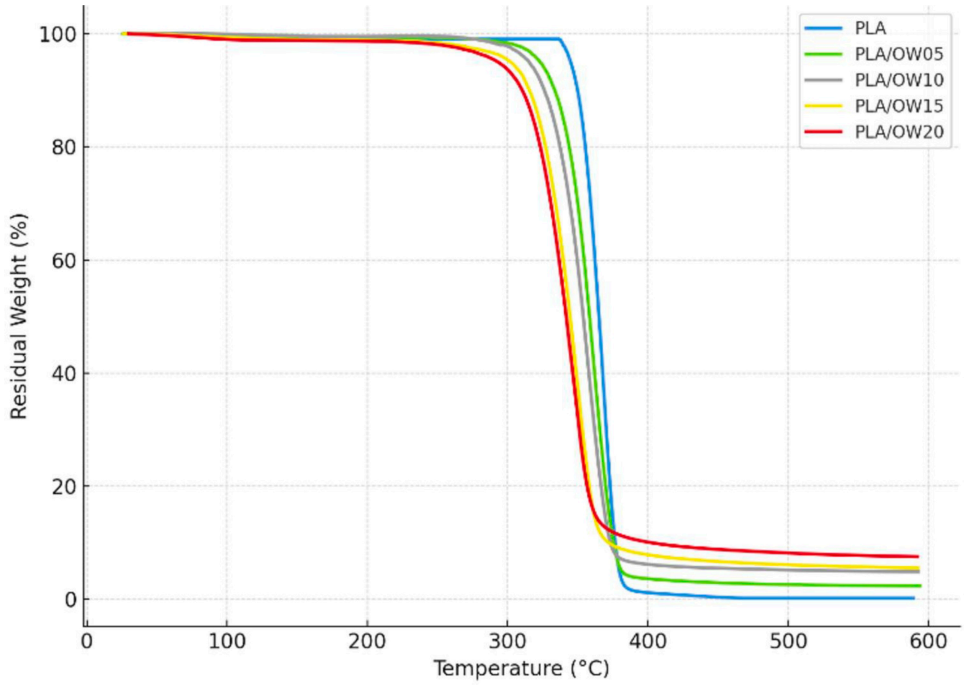

Source: Authors' own work

Table 4 TGA parameters of PLA and PLA/OW composites

Material	$T_{5\%}$ (°C)	T_{max} (°C)	Residue at 580 °C (%)
Neat PLA	344.9	375.9	0.2
PLA/OW05	323.2	361.1	2.4
PLA/OW10	315.3	356.3	4.9
PLA/OW15	302.1	351.3	5.5
PLA/OW20	293.2	348.3	7.5

Source(s): Authors' own work

that higher wood fibre loadings in PLA led to surfaces with more irregular features and fibre pull-outs, attributed to poor interfacial adhesion and increased viscosity during extrusion.

This evolution in surface roughness was consistent with SEM observations, in which cavities, pull-out traces and interfacial heterogeneities became more frequent at higher filler loadings. Therefore, the results confirmed that increasing OW content significantly increased the areal roughness of printed specimens.

Figure 10 shows the variation of the root-mean-square height (S_q) as a function of extrusion temperature for two printing speeds (20 and 200 mm/s). At the lower speed (20 mm/s), S_q remained relatively high across the entire temperature range, ranging from 6.4 to 8.2 μm. A slight reduction was observed from 180°C (7.51 μm) to 240°C (6.40 μm), suggesting improved inter-filament diffusion and surface levelling at intermediate temperatures. However, further increasing the extrusion temperature to 280°C resulted in a pronounced rise

Figure 6 PLA viscosity η^*, storage G′ and loss G″ moduli

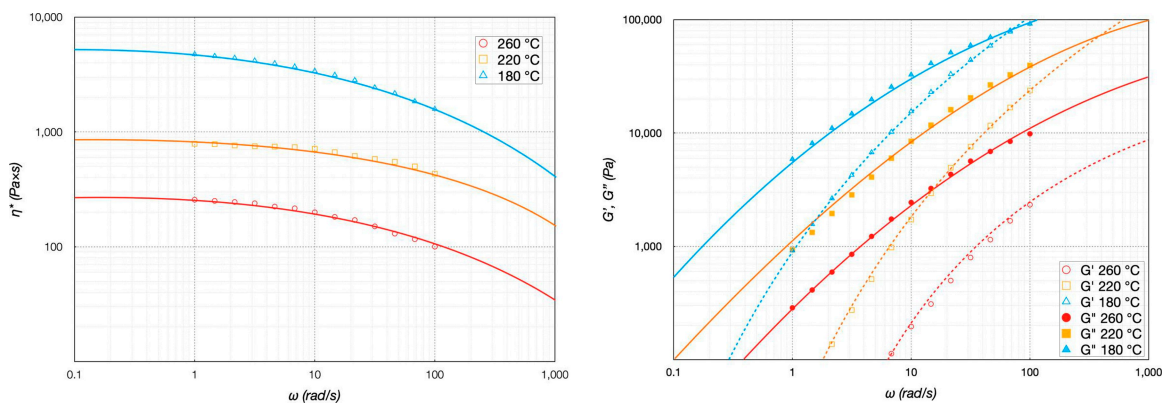

Source: Authors' own work

Figure 7 PLA/OW05 viscosity η^*, storage G′ and loss G″ moduli

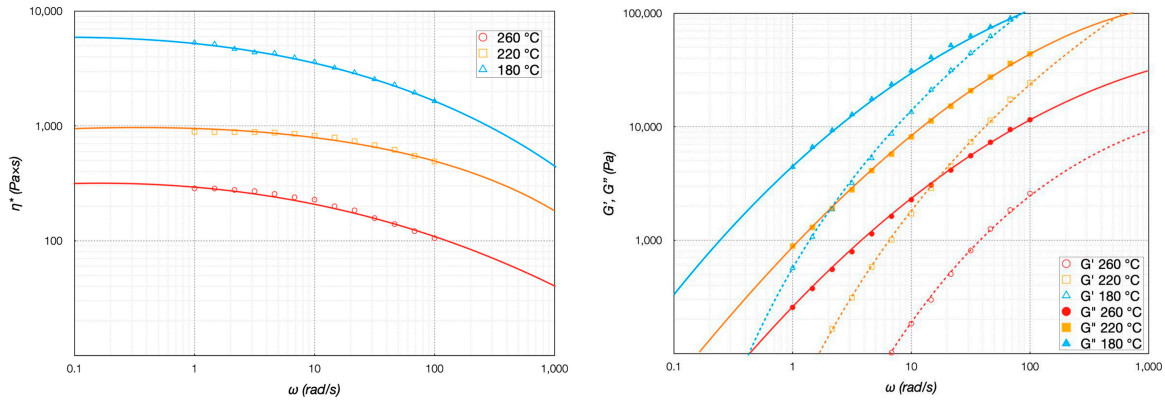

Source: Authors' own work

Figure 8 PLA/OW10 viscosity η^*, storage G′ and loss G″ moduli

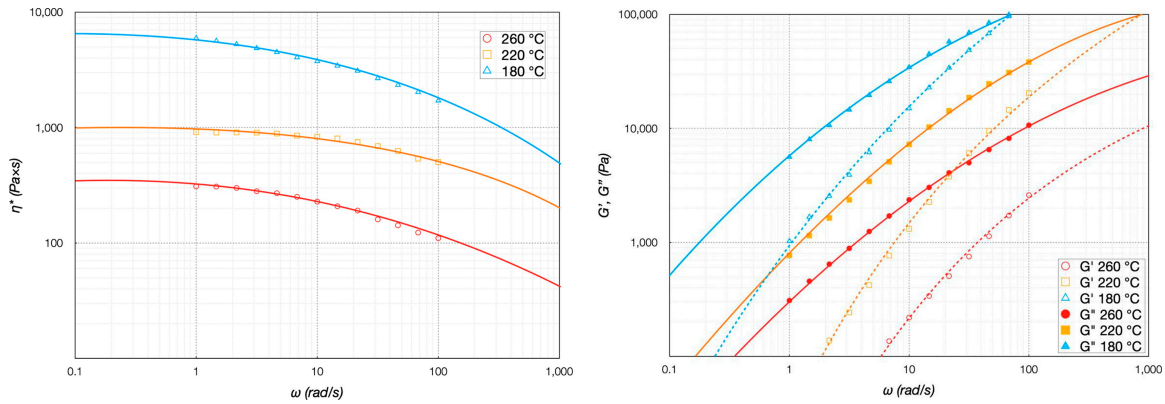

Source: Authors' own work

Figure 9 Surface topography of 3D-printed samples of (a) PLA/OW05 and (b) PLA/OW20

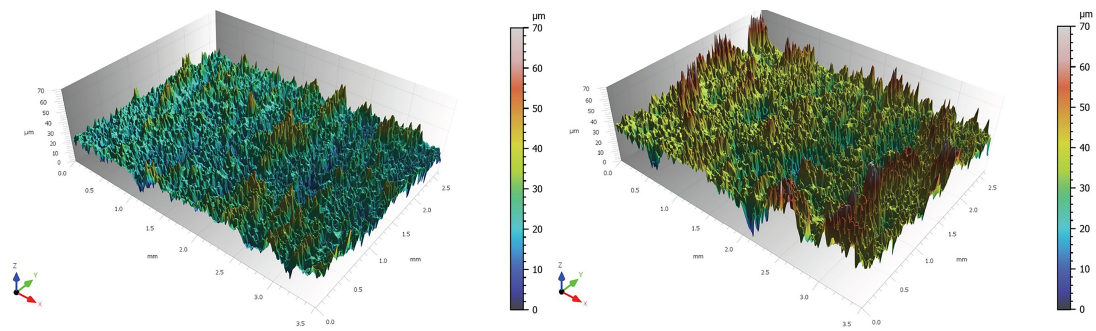

(a) **(b)**

Source: Authors' own work

in S_q (8.20 μm), indicating the onset of surface instability phenomena, such as polymer degradation or excessive flow irregularities, that counteracted the smoothing effect.

At the higher speed (200 mm/s), S_q values were consistently lower than at 20 mm/s, ranging from 5.0–7.02 μm. The lowest roughness was observed between 220 and 240°C (5.20 and 5.08 μm, respectively), indicating an optimal balance between melt fluidity and deposition rate that promoted bead coalescence and decreased asperity height. Beyond this optimum, S_q increased again, reaching 6.50 μm at 280°C, likely

Table 5 Surface parameters of PLA and PLA/OW composites

Parameter	Neat PLA	PLA/OW05	PLA/OW10	PLA/OW15	PLA/OW20
S_a (μm)	3.59	3.76	4.57	5.38	5.39
S_q (μm)	5.01	5.08	6.05	7.41	7.52
S_z (μm)	42.32	48.56	54.23	65.71	76.40

Source(s): Authors' own work

Figure 10 S_q of the printed surfaces of PLA/OW05 as a function of extrusion temperature (180–280°C) at two printing speeds (20 and 200 mm/s)

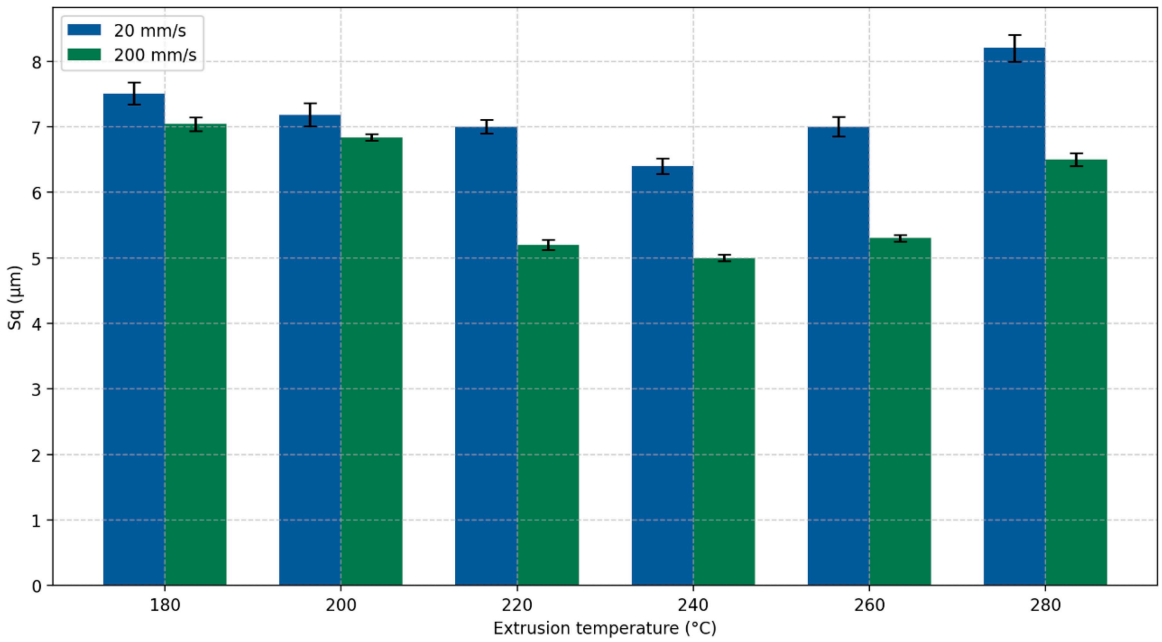

Source: Authors' own work

due to local instabilities at high flow rates and possible degradation of the polymer chains at elevated temperatures.

These results demonstrated that both extrusion temperature and speed exerted a coupled influence on the surface topography of MEX parts. Moderate extrusion temperatures (220–240°C) combined with high deposition speed (200 mm/s) minimized surface roughness, whereas very low or very high temperatures, particularly at low printing speeds, led to higher S_q values. This behaviour was consistent with the roles of temperature in controlling melt viscosity and chain mobility and with the role of speed in governing filament overlap and heat transfer during deposition.

The dependence of S_q on extrusion temperature and printing speed observed in this work was consistent with experimental and modelling studies on MEX. This behaviour also agrees with analytical and experimental roughness descriptions in fused deposition processes, where surface topography is governed by raster geometry and process settings (Boschetto *et al.*, 2013). Previous works demonstrated that inadequate extrusion temperatures limited interfilament diffusion, leading to higher roughness, whereas excessively high thermal input induced surface instabilities (Jiang *et al.*, 2022). Likewise, the trends identified in this study were consistent with another comprehensive review (Golhin *et al.*, 2023), which emphasized that surface quality in MEX was governed by the coupled effects of extrusion temperature and speed. Too low a temperature or excessive printing speed prevented sufficient chain mobility and coalescence. In contrast, high thermal exposure at low speeds promoted sagging and degradation, thereby increasing roughness. In addition, recent studies on recycled PLA fabricated by MEX/FDM have highlighted that build-related parameters significantly affect superficial characteristics and surface-related performance (Altınsoy, 2025; Altınsoy *et al.*, 2025).

3.6 Pyrography analysis

3.6.1 Visual results

Figure 11 shows representative macrographs of the as-printed surfaces of PLA/OW20 produced at different extrusion temperatures (180–280°C) and printing speeds (20 and 200 mm/s). The complete set of surface images for all PLA/OW formulations is provided in the Supplementary material (Section S3).

At lower extrusion temperatures (180°C), the surfaces appeared lighter and the filament raster pattern was clearly visible, particularly at the higher printing speed (200 mm/s). Increasing the extrusion temperature to 240°C resulted in darker surfaces with a more visually uniform appearance,

Figure 11 As-printed surface appearance of PLA/OW20 under different extrusion temperatures (180–280°C) and printing speeds (20 and 200 mm/s)

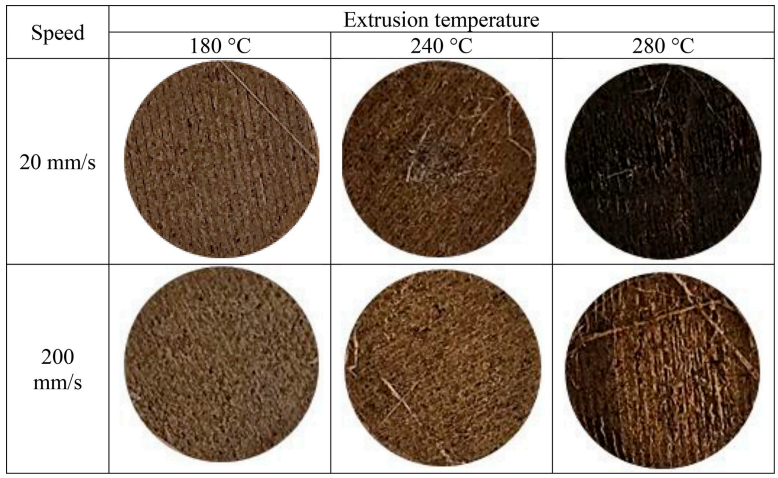

Source: Authors' own work

consistent with improved inter-bead coalescence and reduced visibility of deposition boundaries. However, further increasing the extrusion temperature to 280°C led to over-darkening and, in some cases, surface irregularities and cracks, indicating local thermal instability of the composite under high thermal loads. It should be noted that the extrusion temperature of 280°C is relatively close to the $T_{5\%}$ value measured for the highest-loaded formulation, particularly PLA/OW20. Therefore, especially at low printing speed, this condition should be considered the absolute upper bound of the practical processing window for PLA/OW15 and PLA/OW20, as the longer effective thermal exposure may promote local thermal instability, surface cracking and irregularities.

Printing speed also played a key role. At 20 mm/s, surfaces were generally darker and visually more homogeneous due to the longer effective thermal exposure during deposition, whereas at 200 mm/s the reduced thermal exposure helped preserve lighter tones. These visual trends are consistent with the surface roughness results (Table 5 and Figure 10) and with the reduced thermal stability observed in TGA (Figure 5), confirming that the initial surface condition depends on both processing parameters and composite composition.

Visual inspection of the as-printed surfaces (Figure 11 and Supplementary material – Section S3) indicates that, for a given processing condition, the colour distribution on the exposed surface is generally macroscopically homogeneous, with the main tonal differences occurring between different extrusion-temperature/printing-speed combinations rather than between adjacent deposited layers. Under the most severe conditions, some local visual heterogeneity may appear, likely associated with increased thermal exposure and surface roughness.

3.6.2 Spectral analysis

Figure 12 shows how the CIELAB lightness parameter L^* changed with extrusion temperature for all PLA/OW composites at two printing speeds (20 and 200 mm/s). A clear dependence on both processing parameters and filler content was observed.

At low extrusion temperatures (180–200°C), specimens generally showed high lightness values (L^* 29–34), indicating bright, uniform surfaces. Increasing the extrusion temperature to moderate levels (220–240°C) produced different trends depending on the OW loading. While PLA/OW05 and PLA/OW10 maintained moderate L^* values (30–33), PLA/OW15 and PLA/OW20 exhibited an increase in lightness at 240°C, reaching values up to 35. This suggests improved surface uniformity and reduced scattering due to better filament coalescence.

However, at higher extrusion temperatures (260–280°C), a notable decrease in lightness was observed, especially for PLA/OW15 and PLA/OW20 at low speed, where L^* fell to 24–25. This darkening was due to the thermal degradation of PLA and increased charring of the wood particles when exposed to high temperatures for extended periods, leading to darker surface tones.

Printing speed also had a significant impact. At high speed (200 mm/s), specimens consistently showed higher L^* values compared to those printed at 20 mm/s, indicating that shorter residence time and reduced thermal input helped maintain brightness and prevent excessive darkening. Conversely, at lower speeds, the extended thermal exposure during deposition led to surface darkening, especially at the highest temperatures.

The decrease in L^* observed at higher OW loadings and elevated extrusion temperatures aligned with previous research on PLA/wood composites, which indicated that increasing fibre content and extended thermal exposure darkened the printed surfaces (Taktak *et al.*, 2024; Yang and Yeh, 2020).

The chromatic parameters a^* (green–red) and b^* (blue–yellow) for the PLA/OW composites processed under different extrusion temperatures and printing speeds are shown in Figure 13. In general, a^* values ranged between 6 and 9.5, indicating a shift towards reddish tones, while b^* values (5–10) reflected a tendency towards yellowish hues. This behaviour was typical of lignocellulosic-based composites exposed to elevated temperatures, where partial degradation of hemicelluloses and lignin promoted the formation of chromophores.

At 280°C and low printing speed (20 mm/s), a significant dispersion of coordinates was observed, with some points showing reduced a^* and b^* values (down to 0.5), indicating darkening and loss of saturation due to local carbonization or

Figure 12 Variation of L^* of PLA/OW composites as a function of T and V

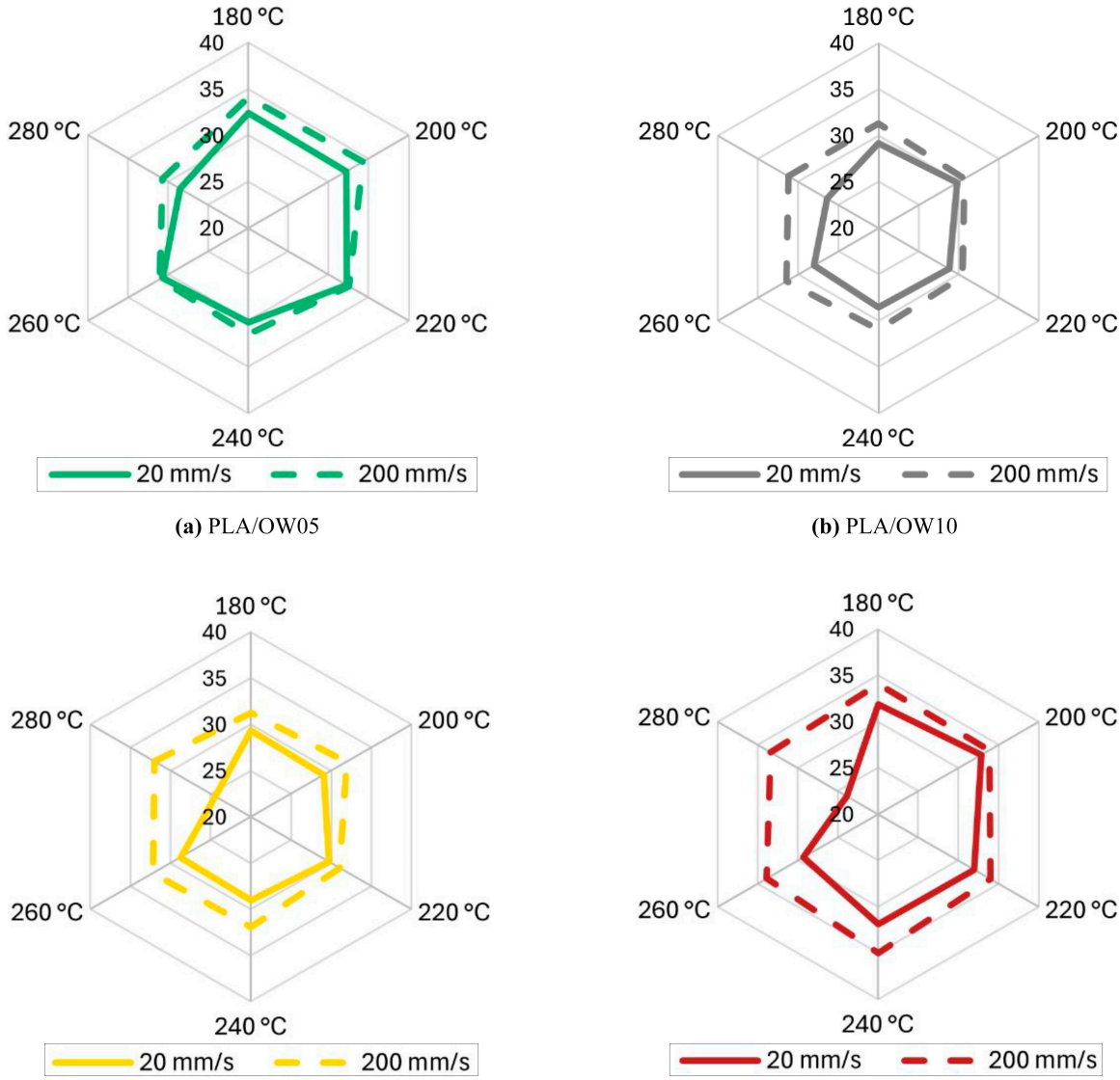

(a) PLA/OW05

(b) PLA/OW10

(c) PLA/OW15

(d) PLA/OW20

Source: Authors' own work

advanced degradation, as noted in Figure 11. At 200 mm/s, these low-b^* outliers disappeared and the a^* and b^* values remained within 6–10, indicating a reduction in severe thermal effects. Increasing OW content lifted b^* values, confirming that the aromatic fractions of olive wood contribute to the final colour, with the highest b^* (≥9) observed for PLA/OW20 at 200 mm/s and 240–260°C.

Although printing speed did not significantly change the mean chromatic coordinates, it affected their dispersion. At 200 mm/s, the data cloud was more compressed, indicating more uniform deposition and shorter thermal exposure. This finding matched the roughness data (Table 5), which showed that lower speeds increased surface irregularities, boosting localized light scattering and colour variability.

The ANOVA results for the colour parameters L^*, a^* and b^* of PLA/OW05 composites are shown in Table 6. These results demonstrate that both extrusion temperature T and printing speed V have statistically significant impacts, with almost all p-values less than 0.001.

For the lightness L^*, extrusion temperature T was the most influential factor, with a sum of squares SS of 30.43 and an F value of 17,848.5, while speed V also had a significant effect ($SS = 8.90$, $F = 5{,}218$). Quadratic effects of temperature $T{\cdot}T$ and the interaction term $T{\cdot}V$ were also significant, indicating non-linear trends and combined effects of processing parameters on brightness. The adjusted R^2 value of 99.99% confirms that the model explains nearly all the variability in L^*.

For the red–green coordinate a^*, extrusion temperature T remained the primary factor ($SS = 10.34$, $F = 1{,}210.5$), followed by quadratic effects $T{\cdot}T$ ($F = 605.9$) and the interaction term $T{\cdot}V$ ($F = 291.5$). The influence of speed V

Figure 13 CIELAB colour coordinates (a^*, b^*) of PLA/OW composites printed at different extrusion temperatures and two printing speeds: (a) 20 mm/s and (b) 200 mm/s

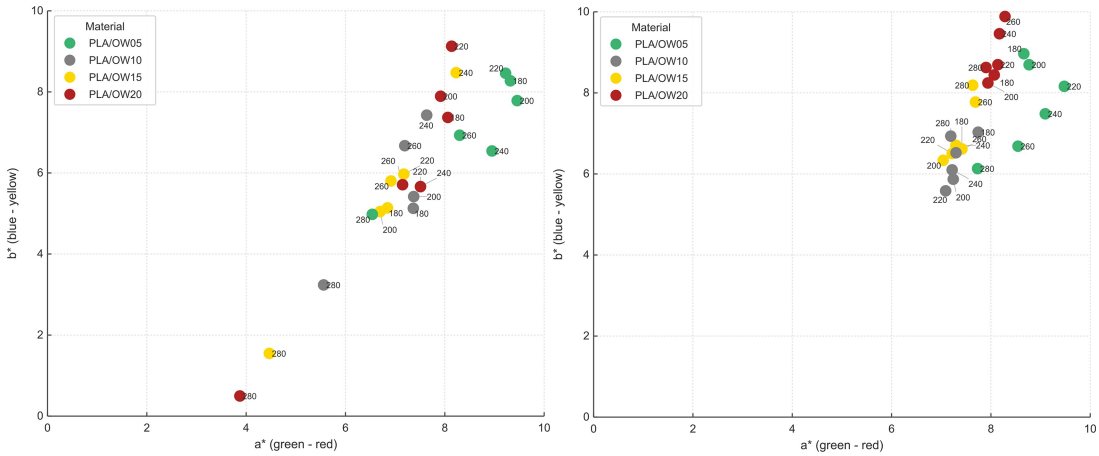

Source: Authors' own work

Table 6 ANOVA for the colour parameters L^*, a^* and b^* of PLA/OW05

Variable	Term.	Sum of squares	Mean square	*F*-ratio	*p*-value
L^*	*T*	30.4328	30.4328	17848.5	<0.001
	V	8.89793	8.89793	5218.53	<0.001
	T·T	1.07763	1.07763	632.02	<0.001
	T·V	0.265598	0.265598	155.77	<0.001
	R^2 (adjusted) = 99.99%				
a^*	*T*	10.335	10.335	1210.46	<0.001
	V	0.123109	0.123109	14.42	0.003
	T·T	5.17281	5.17281	605.85	<0.001
	T·V	2.48903	2.48903	291.52	<0.001
	R^2 (adjusted) = 99.27%				
b^*	*T*	28.1871	28.1871	396,942.13	<0.001
	V	3.73113	3.73113	52,543.23	<0.001
	T·T	0.212414	0.212414	2,991.29	<0.001
	T·V	0.159183	0.159183	2,241.67	<0.001
	R^2 (adjusted) = 99.99%				

Source(s): Authors' own work

alone was relatively minor ($F = 14.4$), though still statistically significant (p value = 0.003). The adjusted R^2 of 99.27% indicated the model's robustness.

For the yellow–blue coordinate b^*, the extrusion temperature T had the most significant impact on variability ($SS = 28.19$, $F = 396{,}942$), with speed V also playing a notable role ($SS = 3.73$, $F = 52{,}543$). Both quadratic $T{\cdot}T$ and interactive $T{\cdot}V$ terms were significant, indicating that the evolution of b^* followed a nonlinear relationship with the processing parameters. The model achieved an adjusted R^2 of 99.99%, demonstrating excellent predictive accuracy.

The analysis confirms that extrusion temperature is the primary determinant of colour coordinates in PLA/OW05, followed by printing speed and their interaction. The high adjusted R^2 values highlight the strong correlation between processing conditions and chromatic response, consistent with the thermal degradation and surface phenomena previously identified.

Polynomial regression models were fitted to predict the colour coordinates (L, a^*, b^*) as a function of extrusion parameters. Extrusion temperature (T) was the most influential predictor, followed by printing speed (V) and their interaction. The full set of estimated regression coefficients is provided in the Supplementary material (Section S4). The resulting empirical models should be interpreted within the tested processing window rather than as universally generalizable relationships.

The response surface plots in Figure 14 illustrate the combined influence of extrusion temperature T and printing speed V on the CIELAB colour parameters of PLA/OW05 specimens. For L^*, a monotonic decrease was observed with increasing temperature, where values dropped from above 34 at 180°C to around 30 at 280°C. This behaviour indicated darkening of the material surface due to enhanced thermal degradation and local carbonization at elevated temperatures.

For a^* (green–red), the model indicated a non-linear trend, with peak values observed approximately between 220 and 240°C, subsequently declining at elevated temperatures. This finding suggests that moderate temperatures facilitate the development of reddish hues. Conversely, excessive heating causes a shift towards lower a^* values, consistent with pigment decomposition and the thermal degradation of lignocellulosic components.

For b^* (blue–yellow), a gradual decrease with rising temperature was observed, indicating a reduction in yellow tones. This was especially clear at higher printing speeds, where b^* values dropped from about 8.5 at 180°C to below 6.0 at 280°C. These trends suggest the progressive breakdown of chromophoric structures within the OW filler, which lowers the yellowish look of the composites.

The response surface analysis confirms that extrusion temperature is the primary factor influencing colour change, while printing speed is a secondary but important variable that affects the degree of thermal degradation and colour variation.

The colour difference parameter (ΔE_{00}), calculated using the CIEDE2000 formula, is shown in Figure 15 for PLA/OW

Figure 14 Response surface plots of T and V effects on the colour parameters: (a) L^*, (b) a^* and (c) b^* of PLA/OW05

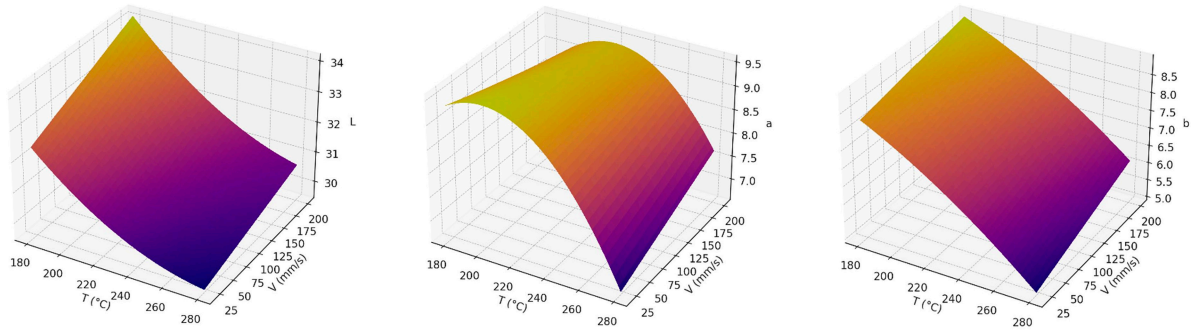

(a) (b) (c)

Source: Authors' own work

Figure 15 Colour difference ΔE00 of PLA/OW composites as a function of extrusion temperature for (a) 20 mm/s and (b) 200 mm/s

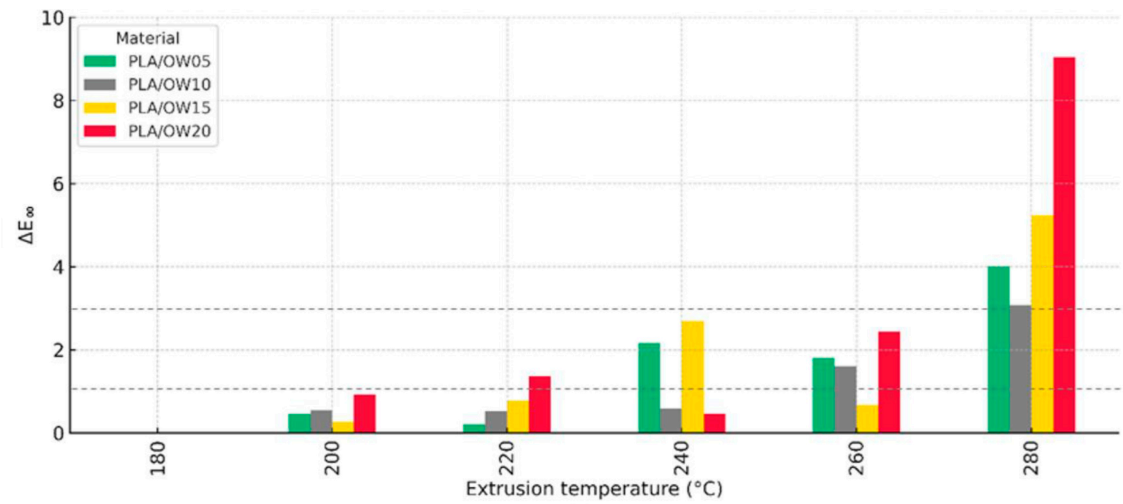

(a)

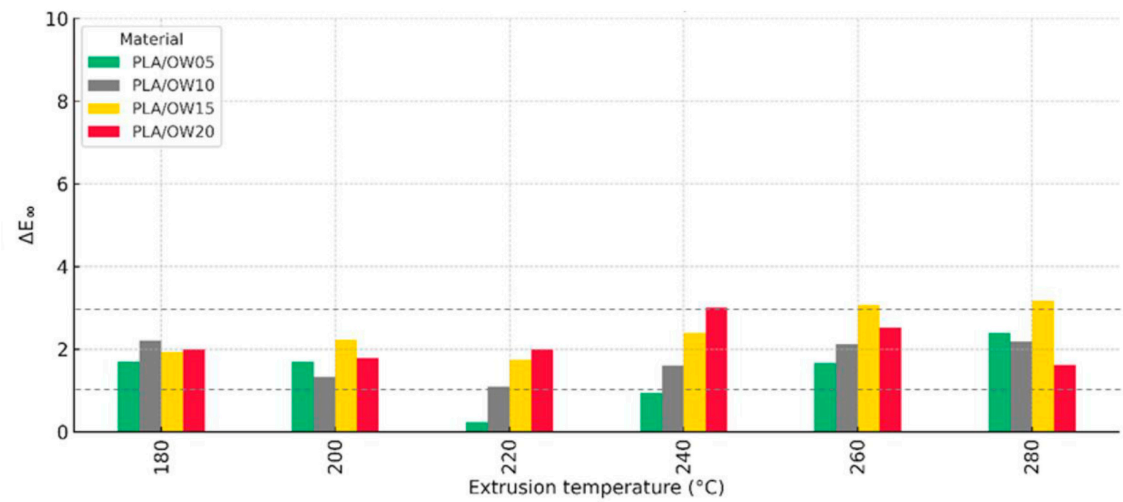

(b)

Source: Authors' own work

composites printed at two speeds (20 and 200 mm/s) across the extrusion temperature range of 180–280°C. The reference values were taken at 180°C and 20 mm/s.

At the lower printing speed of 20 mm/s, ΔE_{00} values showed a clear dependence on temperature and filler content. For all composites, colour differences stayed below 2 at 200–220°C, indicating minor perceptual variations compared to the reference condition. However, above 240°C, ΔE_{00} increased steadily, reaching values over 9 at 280°C for PLA/OW20. These high values reflected substantial, visually noticeable changes caused by enhanced thermal degradation of lignocellulosic components, carbonization effects and the resulting darkening of the specimens.

In contrast, at the higher printing speed (200 mm/s), ΔE_{00} values remained more consistent across the entire temperature range, with most results below 3. This suggested that faster deposition reduced the extent of thermally induced colour change, likely because the material was subjected to lower effective thermal exposure during processing. This behaviour was also consistent with the lower surface roughness measured at higher printing speed, which favoured a more uniform optical response. Overall, the results suggested a qualitative relationship between OW content, surface roughness and colour response. Increasing OW loading promoted a rougher and more heterogeneous surface, while also enhancing the tendency of the material to develop darker tones under elevated thermal exposure. In addition, rougher surfaces may increase local light scattering, thereby contributing to the dispersion of the colour coordinates and the perceptibility of colour differences. These results were also consistent with those obtained in Figures 12–14.

3.6.3 Artifacts of 3D pyrography

Figure 16 shows two proof-of-concept artifacts printed with PLA/OW composites to demonstrate the feasibility of process-controlled 3D pyrography. Noticeable tonal variations were achieved by adjusting extrusion temperature and printing speed, where higher temperatures and lower speeds promoted darker shades due to increased thermal exposure during deposition. Conversely, higher printing speeds helped preserve lighter tones by reducing the effective heating time. These visual outcomes are consistent with the quantified colour trends reported in CIELAB coordinates and ΔE00 (Figure 12–15) and extend recent demonstrations of parameter-driven colour shading in wood filaments to PLA/olive-wood composites with controlled filler content (Moon *et al.*, 2024). In the present case, the visual response was not only reflected in colour changes, but was also linked to surface roughness and processing conditions.

From a practical manufacturing perspective, this approach enables appearance tuning using a single biofilled filament without requiring pigment changes or multi-material switching. As a result, it can potentially reduce the need for multiple coloured filaments, filament changeovers and purge-related waste, while maintaining the intrinsic wood-like aesthetics of PLA/OW materials. This process-driven aesthetic control may be particularly attractive for design-oriented applications in which a wood-like appearance and tonal customization are desirable, such as decorative objects, interior-design elements, architectural mock-ups, customized consumer-product housings, signage and personalized small-series products. In these sectors, the possibility of generating different shades directly during printing using a single biofilled filament may reduce reliance on pigments, post-processing and multi-material switching, while preserving the natural visual character of PLA/OW materials. For practical implementation, the selection of printing conditions should remain within a stable processing window to avoid local overheating, surface cracking or material degradation, particularly at high temperatures and low speeds.

Figure 16 Demonstration of 3D pyrography effect using (a) PLA/OW20 and (b) PLA/OW05

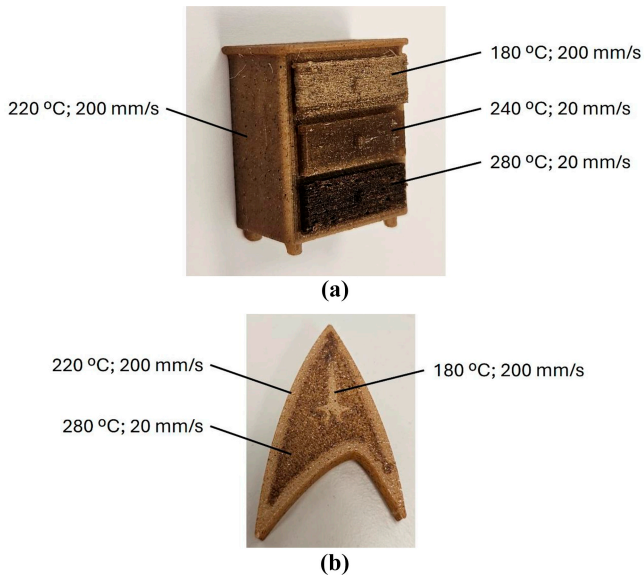

Source: Authors' own work

4. Conclusions

This study analyses the process–appearance relationship of 3D pyrography in PLA/olive-wood composites manufactured by MEX. PLA/OW filaments containing 0–20 Wt.% OW were produced and characterized to assess the relationship between printing conditions, surface texture and CIELAB colour response within the tested processing window.

Morphological and chemical analyses confirmed the incorporation of OW particles into the PLA matrix, together with increasing fracture-surface heterogeneity and characteristic FTIR bands associated with hydroxyl and aromatic lignin groups. Thermal analysis showed that increasing OW content slightly reduced the glass transition temperature and crystallinity of PLA, while decreasing the degradation temperatures and increasing char residue. Rheological analysis revealed higher complex viscosity and storage modulus with OW addition, indicating more restricted melt flow and a narrower practical processing window at higher filler contents.

Surface characterization showed that roughness increased with OW content and was affected by extrusion temperature and printing speed. Within the evaluated range, smoother surfaces were obtained around 220–240°C and 200 mm/s, whereas low printing speed and more severe thermal conditions led to higher S_q values. Colour analysis showed that increasing temperature

caused progressive surface darkening (lower L^*), while higher printing speed reduced this effect by decreasing thermal exposure during deposition. Statistical analysis confirmed strong empirical relationships between processing conditions and colour response within the tested window.

Finally, the proof-of-concept artefacts showed that tonal contrast can be generated directly during printing using a single PLA/OW filament, without post-processing. Overall, the results indicate that 3D pyrography in PLA/OW composites can be controlled through processing parameters and may be useful for applications in which wood-like appearance and surface customization are relevant, particularly in decorative, architectural and product-design contexts.

References

Altınsoy, Ş. (2025), "Effect of print orientation and recycling on the mechanical and tribological properties of 3D-printed PLA polymer materials", *Journal of Mechanical Science and Technology*, Vol. 39 No. 10, pp. 5897-5912, doi: 10.1007/s12206-025-0926-6.

Altınsoy, M., Demirel, M. and Beköz Üllen, N.Ş. (2025), "Effect of the build orientations on mechanical, superficial and bioactivity properties of additively manufactured PLA and recycled PLA filaments", *Journal of Polymer Research*, Vol. 32 No. 11, p. 597, doi: 10.1007/s10965-025-04597-5.

Awal, A., Rana, M. and Sain, M. (2015), "Thermorheological and mechanical properties of cellulose reinforced PLA biocomposites", *Mechanics of Materials*, Vol. 80, pp. 87-95, doi: 10.1016/j.mechmat.2014.09.009.

Bharat, N., Kumar, V., Veeman, D. and Vellaisamy, M. (2025), "Enhancing mechanical properties of 3D-printed PLA/wood composites: a metaheuristic and statistical perspective", *European Journal of Wood and Wood Products*, Vol. 83 No. 3, pp. 809-826, doi: 10.1007/s00107-025-02253-9.

Boschetto, A., Giordano, V. and Veniali, F. (2013), "3D roughness profile model in fused deposition modelling", *Rapid Prototyping Journal*, Vol. 19 No. 4, pp. 240-252, doi: 10.1108/13552541311323254.

Comino, F., Martinez-Sánchez, J.A., Romero, P.E., Gurrado, N. and Spina, R. (2025), "thermo-mechanical properties of polylactic acid/olive wood composite for additive manufacturing", *Materials Research Proceedings*, Vol. 54, *Association of American Publishers*, pp. 2344-2351, 10.21741/9781644903599-253.

Comino, F., Romero, P.E., Molero, E. and Ruiz de Adana, M. (2023), "Experimental evaluation of a 3D printed air dehumidification system developed with green desiccant materials", *Applied Thermal Engineering*, Vol. 227, p. 120393, doi: 10.1016/j.applthermaleng.2023.120393.

Cui, L., Yi, L., Wang, Y., Zhang, Y., Polyák, P., Sui, X. and Pukánszky, B. (2021), "Rheology of PLA/regenerated cellulose nanocomposites prepared by the pickering emulsion process: network formation and modeling", *Materials & Design*, Vol. 206, p. 109774, doi: 10.1016/j.matdes.2021.109774.

dos Santos, N.V., Cavalcanti, D.K.K., Neto, J.S.S., de Queiroz, H.F.M., Banea, M.D. and Cardoso, D.C.T. (2025), "Analysis of voids, interfacial and thermal properties of additively manufactured continuous natural fiber-reinforced biocomposites", *Progress in Additive Manufacturing*, Vol. 10 No. 8, pp. 5401-5422, doi: 10.1007/s40964-024-00913-5.

Ehman, N., Ponce de León, A., Quintero Torres, IN., Vallejos, M.E. and Area, M.C. (2025), "Lignocellulosic agro-forest byproducts as feedstock for fused deposition modeling 3D printing filaments: a review", *Fibers*, Vol. 13 No. 9, p. 124, doi: 10.3390/fib13090124.

Fico, D., Rizzo, D., De Carolis, V., Montagna, F., Palumbo, E. and Corcione, C.E. (2022), "Development and characterization of sustainable PLA/olive wood waste composites for rehabilitation applications using fused filament fabrication (FFF)", *Journal of Building Engineering*, Vol. 56, p. 104673, doi: 10.1016/j.jobe.2022.104673.

Golhin, A.P., Tonello, R., Frisvad, J.R., Grammatikos, S. and Strandlie, A. (2023), "Surface roughness of as-printed polymers: a comprehensive review", *The International Journal of Advanced Manufacturing Technology*, Vol. 127 Nos 3-4, pp. 5511-5553, doi: 10.1007/s00170-023-11566-z.

ISO (2019), "ISO 11664-4:2019. Colorimetry – part 4: CIE 1976 $L^*a^*b^*$ colour space", *International Organization for Standardization*, Geneva.

Jaróg, T., Góra, M., Góra, M., Maroszek, M., Hodor, K., Hodor, K., Hebda, M., *et al.* (2025), "Biodegradable meets functional: dual-nozzle printing of eco-conscious parklets with wood-filled PLA", *Materials*, Vol. 18 No. 13, p. 2951, doi: 10.3390/ma18132951.

Jasiński, W., Szymanowski, K., Nasiłowska, B., Barlak, M., Betlej, I., Prokopiuk, A. and Borysiuk, P. (2025), "3D printing wood–PLA composites: the impact of wood particle size", *Polymers*, Vol. 17 No. 9, p. 1165, doi: 10.3390/polym17091165.

Jiang, S., Hu, K., Zhan, Y., Zhao, C. and Li, X. (2022), "Theoretical and experimental investigation on the 3D surface roughness of material extrusion additive manufacturing products", *Polymers*, Vol. 14 No. 2, p. 293, doi: 10.3390/polym14020293.

Kariz, M., Sernek, M., Obućina, M. and Kuzman, M.K. (2018), "Effect of wood content in FDM filament on properties of 3D printed parts", *Materials Today Communications*, Vol. 14, pp. 135-140, doi: 10.1016/j.mtcomm.2017.12.016. Vol

Khan, I., Amin, J., Abas, M., Babar, M., Mikail Shah, S., Ali, A., Rasheed, A., *et al.* (2025), "Extrusion additive manufacturing of particle-reinforced polymer composites: materials, processes, and applications", *Progress in Additive Manufacturing*, Vol. 10 No. 11, pp. 6415-6453, doi: 10.1007/s40964-025-01201-6.

Lee, C.H., Padzil, F.N.B.M., Lee, S.H., Ainun, Z.M.A. and Abdullah, L.C. (2021), "Potential for natural fiber reinforcement in PLA polymer filaments for fused deposition modeling (FDM) additive manufacturing: a review", *Polymers*, Vol. 13 No. 9, p. 1407, doi: 10.3390/polym13091407.

Le Guen, M.J., Hill, S., Smith, D., Theobald, B., Gaugler, E., Barakat, A. and Mayer-Laigle, C. (2019), "Influence of rice husk and wood biomass properties on the manufacture of filaments for fused deposition modeling", *Frontiers in Chemistry*, Vol. 7, p. 735, doi: 10.3389/fchem.2019.00735.

Liu, Z., Lei, Q. and Xing, S. (2019), "Mechanical characteristics of wood, ceramic, metal and carbon fiber-based PLA composites fabricated by FDM", *Journal of Materials Research and Technology*, Vol. 8 No. 5, pp. 3743-3753, doi: 10.1016/j.jmrt.2019.06.034.

Lo Giudice, V., Faraone, I., Bruno, M.R., Ponticelli, M., Labanca, F., Bisaccia, D., Massarelli, C., *et al.* (2021), "Olive trees by-products as sources of bioactive and other industrially useful compounds: a systematic review", *Molecules*, Vol. 26 No. 16, p. 5081, doi: 10.3390/molecules26165081.

Martínez-Sánchez, J.A., Comino, F., Romero, P.E. and Ruiz de Adana, M. (2025), "Design, development and performance evaluation of a 3D-printed desiccant wheel using poly-lactic acid and wood filaments for sustainable HVAC systems", *Building and Environment*, Vol. 276, p. 112889, doi: 10.1016/j.buildenv.2025.112889.

Mirza, F., Baloor Shenoy, S., Nunna, S., Ramanath Kini, C. and Creighton, C. (2025), "Effect of material extrusion process parameters on tensile performance of pristine and discontinuous fibre reinforced PLA composites: a review", *Progress in Additive Manufacturing*, Vol. 10 No. 5, pp. 3251-3265, doi: 10.1007/s40964-024-00825-4.

Montgomery, D.C. (2004), *Design and Analysis of Experiments*, 6th Edition., Wiley.

Moon, K., Yi, J., Savage, V. and Bianchi, A. (2024), "3D printed pyrography: using wood filament and dynamic control of nozzle temperature for embedding shades of color in objects", *Additive Manufacturing*, Vol. 83, p. 104064, doi: 10.1016/j.addma.2024.104064.

Petinakis, E., Liu, X., Yu, L., Way, C., Sangwan, P., Dean, K., Bateman, S., *et al.* (2010), "Biodegradation and thermal decomposition of poly(lactic acid)-based materials reinforced by hydrophilic fillers", *Polymer Degradation and Stability*, Vol. 95 No. 9, pp. 1704-1707, doi: 10.1016/j.polymdegradstab.2010.05.027.

Sharma, G., Wu, W. and Dalal, E.N. (2005), "The CIEDE2000 color-difference formula: implementation notes, supplementary test data, and mathematical observations", *Color Research & Application*, Vol. 30 No. 1, pp. 21-30, doi: 10.1002/col.20070.

Sheng, D.D.C.V., Yahya, M.N.B., Din, N.B.C., Wong, K.Y., Asyraf, M.R.M. and Sekar, V. (2024), "Potential of wood fiber/polylactic acid composite microperforated panel for sound absorption application in indoor environment", *Construction and Building Materials*, Vol. 444, p. 137750, doi: 10.1016/j.conbuildmat.2024.137750.

Spina, R. (2025), "Surface appearance of poly lactic acid due to variations in material extrusion processing parameters", *Scientific Reports*, Vol. 15 No. 1, p. 22684, doi: 10.1038/s41598-025-14484-0.

Sultana, J., Rahman, M.M., Wang, Y., Ahmed, A. and Xiaohu, C. (2024), "Influences of 3D printing parameters on the mechanical properties of wood PLA filament: an experimental analysis by Taguchi method", *Progress in Additive Manufacturing*, Vol. 9 No. 4, pp. 1151-1165, doi: 10.1007/s40964-023-00516-6.

Sun, Q., Rizvi, G.M., Bellehumeur, C.T. and Gu, P. (2008), "Effect of processing conditions on the bonding quality of FDM polymer filaments", *Rapid Prototyping Journal*, Vol. 14 No. 2, pp. 72-80, doi: 10.1108/13552540810862028.

Taktak, I., Mansouri, A., Guerfali, M., Ayadi, I., Souissi, S., Gargouri, A., Etoh, M.A., *et al.* (2024), "Active bio composites films based on PLA/olive wood flour (*Olea europaea L.*)/cinnamon essential oil", *Polymer Bulletin*, Vol. 81 No. 1, pp. 719-737, doi: 10.1007/s00289-023-04737-1.

Taktak, I., Mansouri, A., Souissi, S., Etoh, M.A. and Elloumi, A. (2023), "Biocomposites films based on polylactic acid and olive wood-flour: investigation on physical, thermal and mechanical properties", *Journal of Elastomers & Plastics*, Vol. 55 No. 4, pp. 597-612, doi: 10.1177/00952443231165426.

Tao, Y., Wang, H., Li, Z., Li, P. and Shi, S.Q. (2017), "Development and application of wood flour-filled polylactic acid composite filament for 3d printing", *Materials*, Vol. 10 No. 4, p. 339, doi: 10.3390/ma10040339.

TotalEnergies Corbion (2022), "Luminy® LX175: technical data sheet", available at: http://totalenergies-corbion.com/wp-content/uploads/2025/02/pds-luminy-lx175-20220722.pdf, (accessed 22 July 2022)

Travieso-Rodriguez, J.A., Jerez-Mesa, R., Llumà, J., Gomez-Gras, G. and Casadesus, O. (2021), "Comparative study of the flexural properties of ABS, PLA and a PLA–wood composite manufactured through fused filament fabrication", *Rapid Prototyping Journal*, Vol. 27 No. 1, pp. 81-92, doi: 10.1108/RPJ-01-2020-0022.

Turner, B.N., Strong, R. and Gold, S.A. (2014), "A review of melt extrusion additive manufacturing processes: I. Process design and modeling", *Rapid Prototyping Journal*, Vol. 20 No. 3, pp. 192-204, doi: 10.1108/RPJ-01-2013-0012.

Yang, T.C. and Yeh, C.H. (2020), "Morphology and mechanical properties of 3D printed wood fiber/polylactic acid composite parts using fused deposition modeling (FDM): the effects of printing speed", *Polymers*, Vol. 12 No. 6, p. 1334, doi: 10.3390/POLYM12061334.

Yue, Z., Wang, H., Zhang, M. and Wang, M. (2022), "Mechanical, thermal and rheological properties of polylactic acid (PLA)/epichlorohydrin modified pine wood flour (EWF) composites", *European Journal of Wood and Wood Products*, Vol. 80 No. 5, pp. 1111-1120, doi: 10.1007/s00107-022-01810-w.

Zhou, J., Wang, B., Xu, C., Xu, Y.Z., Tan, H., Zhang, X. and Zhang, Y. (2022), "Performance of composite materials by wood fiber/polydopamine/silver modified PLA and the antibacterial property", *Journal of Materials Research and Technology*, Vol. 18, pp. 428-438, doi: 10.1016/j.jmrt.2022.02.113.

Supplementary material

The supplementary material for this article can be found online.

Corresponding author

Francisco Comino can be contacted at: francisco.comino@uco.es